

Effective Ways to Stabilize Polysulfide Ions for High-Capacity Li–S Batteries Based on Organic Chalcogenide Catholytes

Georgios Nikiforidis,^[a, b] Julie Pires,^[a] Satyajit Phadke,^[a] and Mérièm Anouti*^[a]

Given the great promise of lithium-sulfur (Li–S) batteries as next-generation high-capacity energy storage devices, this feature article investigated critical parameters of the cathode, such as pretreatment of elemental sulfur (sublimed, polymerized, and crystallized), size of sulfur particles (19 vs. 35 μm) and aptness of current collector (aluminium vs. carbon paper). At the same time it also demonstrated the applicability of polychalcogenide-based catholytes (e.g., diphenyl disulfide and diselenide) that exhibited a record specific capacity

(3000 mAhg⁻¹ at a C/5 rate) and an energy density of 1853 WhKg⁻¹. From tweaking the sulfur nature in the cathode, where small-sized polymerized sulfur was found to promote the carbon-sulfur bond on the surface of carbon nanotubes, to trapping the polysulfide ions to formulate organochalcogenide-based catholytes, our study provided fundamental insights into key battery performance parameters as well as sulfur-polysulfide electrochemistry, inspiring future designs of such battery systems and more.

Introduction

The quest to decarbonize the economies of developed countries has led to the rapid advancement and deployment of energy storage systems. Efficient and rechargeable energy storage devices can successfully and promptly integrate renewable energy sources into power systems for transportation, portable, and stationary backup power.^[1] Li-ion batteries (LIB) exhibit high power density (PD_{max} ~ 300 Whkg⁻¹),^[2] a long cycle lifetime, and thus are widely used to fulfil the sustained growth in electronic devices and electric vehicles.^[3] Yet, the active materials of conventional LIBs involve mined elements such as nickel, manganese, and cobalt. Their safe disposal and recycling pose technical challenges as the volume of global battery manufacturing continues to increase.^[4] In addition, most LIB cathodes (materials based on transition metal oxides) operate at high voltages (> 4.0 V), where electrolyte decomposition triggers oxygen loss and capacity fade.^[5] Therefore, there is an increasing effort to substitute such expensive and unsustainable materials by adopting the “beyond Li-ion” paradigm, e.g., other alkaline metal batteries and alternate electroactive materials at the cathode, with oxygen and sulfur being eligible candidates.

Both are readily available^[6] and hold superior theoretical energy density (e.g., 3505 Whkg⁻¹ for a Li-air battery based on 2Li + O₂ → Li₂O₂)^[7] and specific capacity (e.g., 1168 mAhg⁻¹ for Li₂O₂,^[7] and 1672 mAhg⁻¹ for mineral sulfur,^[8] subject to S₈ + 16Li → 8Li₂S). The above traits enable them to reduce the weight of electronic devices, prolong the driving range of electric vehicles, potentially reduce cost, and improve safety.^[9]


Lithium-sulfur (Li–S) batteries have markedly progressed during the last decades and are currently being commercialized. Examples include aerospace applications such as HAPS (High-Altitude Pseudo-Satellite) drones and marine,^[10] while companies such as Oxis Energy, Zhongke Paisi and Sion Power have streamlined 400 WhKg⁻¹ Li–S batteries for kWh-level applications.^[11] These cells comprise a carbon-sulfur (C/S) cathode, a separator with an active or solid-state electrolyte^[12] tailored with a ceramic composite^[13] that enables ionic diffusion, and at the anode, passivated metallic lithium. The electrolyte is the heaviest component of the cell and represents the most critical lever in the cell's specific energy.^[14] To achieve a high energy density and long cycle life, the electrolyte, typically an ether or carbonate-based solvent to (elemental) sulfur mass ratio, *r*, should be minimized [Eq. (1)].^[15]


$$r \sim \frac{5 \mu\text{L of electrolyte}}{1 \text{ g of sulfur}} \quad (1)$$

During cell operation, the polysulfides initially formed at the cathode dissolve into the electrolyte during discharge. The soluble long-chain polysulfides (i.e., S_{2x}²⁻; x = 3–4) diffuse through the separator to the lithium anode and are reduced to short-chain polysulfides (i.e., S_x²⁻; x < 4) and insoluble Li₂S₂ or Li₂S through parasitic reactions with the lithium metal.^[14] During charge, the reduced sulphides recombine with dissolved polysulfides and diffuse back to the cathode, where they are re-oxidized. This multi-step reduction of sulfur enables the

[a] Dr. G. Nikiforidis, Dr. J. Pires, Dr. S. Phadke, Prof. M. Anouti
Laboratoire PCM2E
Université de Tours
Parc de Grandmont, 37200 Tours, France
E-mail: meriem.anouti@univ-tours.fr

[b] Dr. G. Nikiforidis
Institute for Materials Discovery
University College London
Roberts Building, Malet Place, London, WC1E 7JE, UK

 Supporting information for this article is available on the WWW under <https://doi.org/10.1002/celec.202200571>

 © 2022 The Authors. ChemElectroChem published by Wiley-VCH GmbH. This is an open access article under the terms of the Creative Commons Attribution License, which permits use, distribution and reproduction in any medium, provided the original work is properly cited.

formation of intermediate polysulfide species (trapped in the porous matrix during discharge) that repeatedly “shuttle the polysulfide ions” between the negative and positive electrodes and, along with parasitic reactions, propagate active material loss, shorten the cell life and hinder the battery’s performance (i.e., low coulombic efficiency and specific capacity retention).

In that regard, a great deal of research has been conducted on the design of sulfur cathodes holding different morphologies (e.g., nanostructured host materials based primarily on carbon, graphene, and conductive polymers).^[14] Such strategies, aim to encapsulate the active material, confine the soluble species formed during the electrochemical redox reaction and mitigate their diffusion.^[10,16,17] While there has been some success on a laboratory scale,^[18] such fabrication methods are complex, costly, and often inapt for scale-up. Besides, they compromise the battery’s energy density by reducing the sulfur loading and increasing the amount of electrochemically inert materials.^[14] Following a material-based approach does not avert the dissolution of long-chain polysulfides and, in turn, the shuttle effect and parasitic reactions between polysulfides and lithium. Another approach entails electrolyte optimization, where the aforementioned challenges could be addressed more effectively. It typically involves tweaking the solvents and salts of the catholyte, introducing additives, or using solid electrolytes. This plan of action aims to inhibit polysulfide shuttling, improve the surface of lithium and enhance Li^+ diffusion.^[14,19] In this vein, the addition of organic polysulphides (e.g., thiols and disulfides)^[20] is a promising way because it can i) mitigate the redox shuttle phenomenon and ii) contribute additional capacity to the cell. Yet, the interactions of the organic and mineral polysulphide species with the various elements of the batteries, namely lithium metal, separator, electrolyte salt and solvent, and the composition of the C/S cathode, have not been extensively analyzed.

To this end, starting from a standard ether electrolyte comprising DOL/DME (1,2-dimethoxyethane and 1,3-dioxolane), $0.25 \text{ mol L}^{-1} \text{ LiNO}_3$ (lithium nitrate), and $1 \text{ mol L}^{-1} \text{ LiTFSI}$ (lithium bis(trifluoromethanesulfonyl)imide), we evaluate different cell performance parameters, namely the crystallinity of sulfur, the size of sulfur particles and the suitability of the current collector. In addition, we report the superior performance of a Li–S battery in the presence of organic polychalcogenides (PhX_2Ph ; $\text{X} = \text{S}, \text{Se}$) with a record high specific capacity (i.e., 3000 mAh g^{-1} at a C/5 rate), paving the way for further research on catholyte formulation.

Experimental Section

Chemicals and materials

1,2-Dimethoxyethane (DME), 1,3-dioxolane (DOL), lithium bis(trifluoromethane-sulfonyl)imide (LiTFSI) and LiNO_3 (lithium nitrate) were purchased from Sigma–Aldrich. The solvents were dried with activated 4 Å molecular sieves (Merck) for 48 hours prior to use. Diphenyl disulfide (Ph_2S_2 , Sigma–Aldrich) and diphenyl diselenide (Ph_2Se_2 , Sigma–Aldrich) were dried at 30°C under vacuum for 24 h and then stored in an argon-filled glovebox. The appropriate

amounts of Ph_2S_2 and Ph_2Se_2 were added to the standard ether electrolyte (i.e., $0.25 \text{ mol L}^{-1} \text{ LiNO}_3$ and $1 \text{ mol L}^{-1} \text{ LiTFSI}$ in DOL/DME, (volume ratio: 1/1) to reach concentrations between 0.1 and 1.0 mol L^{-1} . The electrolytes were prepared in an Ar-filled glovebox with controlled moisture and oxygen level ($<0.1 \text{ ppm}$). Lithium metal (99% trace metals basis) was purchased from Sigma–Aldrich. The punched lithium disks (0.75 mm thickness) were soaked overnight in a solution containing 1 mol LiNO_3 and DOL/DME before being introduced to the cell.

Cathode formulation

The C/S nanocomposites were supplied by Arkema© (France). They were prepared by impregnating sulfur into microsized spherical graphitized and nanoporous carbon-containing CNT^[21] (following the Oxis Energy Ltd. patent.^[22] The C/S blend nanocomposite was mixed in a 2:1 weight ratio with carbon additive (Ketjen Black, EC-600JD, Nanografi) in a mortar and pestle for 2 h. Polyvinylidene fluoride (PVDF, Sigma–Aldrich) was dissolved in 1-methyl-2-pyrrolidone (NMP, Merck) to form a 2 wt% PVDF-NMP mixture. Different weight ratios of the (S/C)/KB/PVDF ink were formulated, viz. 60:30:10, 70:20:10, and 80:10:10. The slurry was coated onto pre-cut disk current collectors (14 mm diameter) of either carbon paper (Toray, 190 µm thickness) or aluminum mesh (Dexmet Corporation, 50 µm thickness). Before coating, the aluminum mesh was etched for 6 s in fuming hydrochloric acid (37%) to remove the aluminum oxide, followed by a rinse with isopropanol. The coated electrodes were dried in air and then at 60°C under vacuum for 12 h. The sulfur loading on the substrate was between 1.2 and 1.5 mg cm^{-2} . Based on a previous study that examines the correlation between the BET (Brunauer, Emmett, and Teller) surface, pore size distribution, nature of carbon, and first discharge capacity,^[23] the BET surface area of the C/S electrode lies between 12 and $11 \text{ m}^2 \text{ g}^{-1}$, and the pore volume among 0.12 and $0.13 \text{ cm}^3 \text{ g}^{-1}$.

Electrochemical experiments

2032 coin cells (Hosen, Japan) were assembled using lithium metal as the negative electrode and the C/S electrode as the positive electrode in an Argon-filled glove box with separators in-between (GF/C, Whatman®). The volume of added electrolyte was 120 µL. The cells underwent a 6 h conditioning process in the glovebox after assembly and were cycled at various C rates ($1\text{C} = 1675 \text{ mA/g}_{\text{sulfur}}$) on a multichannel potentiostat-galvanostat (Biologic VMP3, France) within 1.8–2.7 V. A hydraulic disassembling machine (MSK-110D, MTI corporation) was used to disassemble the cells. Potentiostatic electrochemical impedance spectroscopy (EIS) was performed on the same Biologic multichannel potentiostat-galvanostat. The oscillating amplitude was fixed at 10 mV, and the impedance spectra were collected between 0.5 MHz and 0.01 Hz in a logarithmic manner, at ten points per decade.

Physicochemical characterization

The thermal stability and crystallinity of sulfur were recorded by differential scanning calorimetry (DSC) using a Perkin-Elmer DSC 4000 coupled with an Intercooler VLT-100 2P. The heating rate was 5°C min^{-1} , and the temperature range spanned from 0 to 130°C under nitrogen flow, at 20 ml min^{-1} . XRD (X-ray Diffraction) analysis of sulfur comprising different particle sizes was carried out with an X-ray diffractometer (D8 Advance, Bruker). The wavelength of the Cu K_α radiation, λ , was 1.54 nm. The surface morphology of the C/S cathode was characterized by scanning electrode microscopy (SEM, FEI Nova) with an accelerating voltage of 3 kV. The cross-sectional image of the C/S cathode was examined with a focused ion beam

(FIB) SEM (FEI Helios NanoLab 400S) using a Ga⁺ ion source. The Raman spectra of the C/S cathode were obtained inVia™ confocal Raman microscope (Renishaw) under a 532 nm laser excitation. The deconvolution of the D and G bands was done by Lorentzian fitting. The XRD spectra of the C/S electrode and CNT were collected from a D8 Advance (Bruker) using Ni filtered Cu K α (1.54 Å, generator: 40 kV, 40 mA) radiation, equipped with a Lynxeye detector (2 θ range from 10° to 90° in continuous mode and step size of 0.02). Thermogravimetric analysis (TGA) curves of the C/S electrode were recorded on a TGA 4000 PerkinElmer system under a nitrogen atmosphere, coupled with a cooling system (Haake 25, ThermoScientific). The heating rate was 10 °C min⁻¹, and the temperature range spanned from 25 to 700 °C under nitrogen flow (19.8 mlmin⁻¹). The contact angle of the C/S cathode was measured by a contact angle tester (DSA10-Mk2, KRÜSS GmbH Germany) at room temperature through the sessile drop method. A four-point probe system (Ossila, T2001A3) determined the sheet resistance and mean conductivity of the C/S cathode. The polyselenide electrolyte was monitored by optical spectroscopy (PerkinElmer, Lambda 750S). The solutions were placed in a quartz glass cuvette (Ossila, JGS3 UV), diluted with DOL-DME in the glovebox, sealed, and taken out for measurement.

Results and Discussion

Pretreatment of sulfur (crystallinity) on the C/S composite

The lithium polysulfides are electrochemically active upon Li-S cell assembly at an idle state (Figure S1 and Table S1). After the

first discharge, the sulfur reduction renders the polysulfide ions S_x²⁻ (x=8-2) chemically and electrochemically active. During charge, the oxidation of ions enables them to be redeposited either totally or partially onto the carbon matrix. This deposit follows an electrochemical mechanism different from the one used to formulate the initial cathode electrode (i.e., trapped dissolved polysulfides that accommodate volume change during cycling^[24]), highlighting the infiltration of sulfur into the carbonaceous materials. It has been reported that the most stable crystal type of elemental sulfur is orthorhombic α -sulfur,^[25] while regular hexagonal in a single crystal plane is formed at the carbon matrix of the cathode.^[26] This crystal type can mitigate polysulfide shuttling and transform the polysulfide intermediates into insoluble sulfur deposited on the carbon surface at the cathode.^[27]

In this context, premeditating the sulfur crystallinity for cathode formulation is crucial for the long-term operation of the Li-S cell. Figure 1a shows the DSC graphs of different sulfur powders prepared and supplied by Arkema®, namely sublimed, crystallized, and polymerized. The crystallinity of sulfur is determined by the ratio of the two endothermic peaks within the 95–120° temperature window (i.e., $\frac{S_1}{S_1+S_2}$), attributed to phase transition and melting of elemental sulfur. The first broad peak (S₁, 108–109 °C) describes the crystalline nature of sulfur, while the second one (S₂, 115 °C) is ascribed to the amorphous part of sulfur.^[28] The sublimed sulfur revealed the highest crystallinity (96%, the conductivity of crystalline sulfur is ca. 10⁻²⁷ Sm⁻¹),

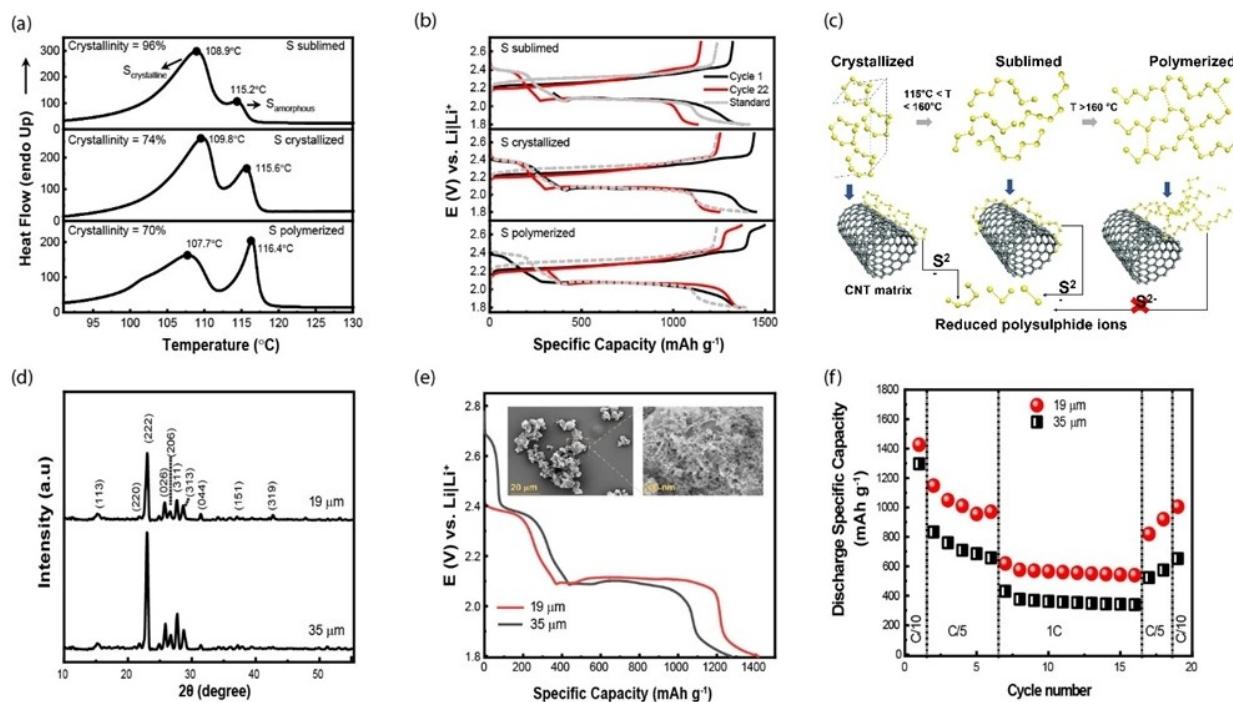


Figure 1. a) Dynamic DSC heat flow graphs of pretreated sulfur powders. b) Galvanostatic discharge and charge profiles (1st and 22nd cycles) of the Li-S cells containing the pretreated sulfur in the cathode. The current is C/10. c) Schematic showing the sulfur deposition mechanism on the carbon nanotubes contingent on the properties of each pretreated sulfur powder. The structure of the elemental octasulfur crystal is rhombohedral. d) XRD spectra of sulfur powders containing different sizes. e) Galvanostatic discharge profiles of Li-S cells containing sulfur particles of different sizes. Inset shows SEM micrographs of sulfur particles at $\times 1000$ and $\times 30000$ magnification. f) Rate performance of Li-S cells under different sulfur particle sizes. The current densities are the same for both charge and discharge in each cycle. The performance is measured at various current densities in an electrolyte comprising DOL/DME, 0.75 mol L⁻¹ LiTFSI, and 0.25 mol L⁻¹ LiNO₃. The operating temperature is 25 °C.

followed by crystallized and polymerized sulfur (74 and 70%). Typical galvanostatic charge-discharge protocols evaluated the cell's performance under a standard electrolyte comprising DOL/DME (1/1, by volume) 0.75 mol L⁻¹ LiTFSI and 0.25 mol L⁻¹ LiNO₃. The stability of the imide salt (LiTFSI) helps the formation of polysulfides and radical species^[29] during cell operation. Further, it shows superior performance at high C-rates compared to other imide salts^[30] (e.g., LiFSI, Figure S2). At the same time, LiNO₃ hinders the polysulfide shuttle mechanism by forming a protective film on the lithium metal surface through the NO₃⁻ anions on or in the proximity of the carbon surface in the sulfur cathode.^[31] Similar ether-based formulations have been reported in Li-S room temperature cells^[32] and in our previous studies with great success.^[20a,b]

Figure 1b displays the GCD graphs of the 1st and 22nd cycles at a C/10 rate following the layout of Figure 1a. The cathode formulation is 60% C/S mixture, 30% Ketjen black, and 10% PVDF dissolved in NMP. In all first discharge curves, elemental octasulfur (S₈) is converted to intermediate polysulfides (S₄²⁻ and S₃²⁻) through the first discharge plateau (or sloping region) at 2.4 V vs. Li|Li⁺. It is then followed by a second long and stable plateau (~2.05 V vs. Li|Li⁺ for the standard ether electrolyte) in the direction of the end of discharge (i.e., >1100 mAhg⁻¹_{sulfur}), where the formation of low-order polysulfides occurs. In particular, formed S₂²⁻ gets reduced to metastable polysulfide species S²⁻ that chemically re-oxidize to S₃²⁻ and S₄²⁻ and produce insoluble Li salts such as Li₂S₂ and Li₂S.^[20a] The sloping part of the second discharge plateau is mitigated for the cells containing crystallized and sublimed sulfur (Figure 1b) and is almost non-existent in the case of polymerized sulfur (i.e., no premature cell voltage drop).

Typically, sulfur forms crystals at temperatures below 160 °C. At elevated temperatures (>160 °C), the octasulfur chains open. Then, the deposit is more homogeneous and follows the structure of an octasulfur chain. The sulfur polymerizes with prolonged heat treatment and is adsorbed on the carbon surface, forming strong C-S bonds that do not detach from the structure. Indeed, the C-S bond (E_{binding} = 261 kJ mol⁻¹) is stronger than the S-S bond (E_{binding} = 226 kJ mol⁻¹).^[25] The polymerized sulfur forms C-S bonds on the carbon surface (i.e., disulfide and trisulfide bridges with the carbon nanotubes in the matrix, Figure 1c) that impede the formation of highly reducing S₂⁻ ions and Li₂S, both linked with an abrupt voltage drop at the end of discharge. Previous work corroborates the above rationale. For example, by carbonizing organic/polymer materials and sulfur at 600 °C, sulfur was decomposed into S₂ and S₃ and bonded to carbon and other elements in the carbon matrix,^[33] forming a molecular-level dense C/S composite.^[15] The cell containing the polymerized sulfur at the cathode produces the highest specific capacity, not taking into account the initial forming cycle. At a C/10 rate, it reaches 1350 mAhg⁻¹ (Figure S3), and after 22 deep cycles (C/5, 1C, C/10), the cell retains 99% of the total capacity. Such a performance is ascribed to the C/S-polymerized composite encapsulating Li₂S in the CNT matrix at the end of charge, boosting sulfur utilization.^[34] Besides, throughout the cycling protocol, these specific capacities were superior to those of the reference cell that uses

commercial sulfur mixed after fine grinding with carbon black (grey line Figure 1b and Figure S3).

Effect of sulfur powder size

Aside from the pretreatment of sulfur, its size is equally important when incorporated into the cathode slurry. The C/S nanocomposite is typically prepared by impregnating sulfur into a microsized spherical nanoporous carbon. Two sulfur sizes (i.e., 35 and 19 μm) provided by Arkema® are investigated here. The well-resolved diffraction peaks between 23 and 29° of the XRD plot (Figure 1d) are indexed to the orthorhombic structure from the cyclooctasulfur molecules. No other phase is found, verifying the presence of pure monoclinic sulfur. The sulfur content in CNT was ca. 37.15% (Figure S4a), leaving the surface covered by the (hydrophobic) fibrous network of CNT (cathode formulation 70:20:10, inset of Figure 1e and Figures S4b and S4c). Standard galvanostatic tests exposed a ×1/3 higher discharge specific capacity for the cell containing lower powder size (owing to an elongated first discharge plateau, Figures 1e and 1f), suggesting a higher active surface area (i.e., greater sulfur utilization). An ×1.85 reduction in powder size can increase the surface area by a factor of four (assuming spherical particles, $s_A = 4\pi r^2$, then if $\frac{r_1}{r_2} = 2 \rightarrow \frac{s_1}{s_2} = \left(\frac{r_1}{r_2}\right)^2 \sim 4$, where r describes the radius of the sulfur powder). Furthermore, the plateau observed at 2.7 V (Figure 1e) is ascribed to the kinetically slower initial formation of S₈²⁻ ions. The first stage of sulfur reduction proceeds by two successive electrochemical-chemical (EC) steps.^[35] Equation (2) (step 1, E=2.7 V vs. Li|Li⁺)^[35] competes with the slow disproportionation of S₈²⁻ ions in conformity with Equation (3) (step 2, E=2.7 V vs. Li|Li⁺),^[35] overall [Eq. (4)].



The radical anions S₃⁻ are more challenging to reduce, leading to lower sulfur reduction voltages. The voltage of the first reduction plateau of sulfur depends on the kinetics of the electronic transfer of the faradaic reaction (step 1) and the kinetics of the chemical disproportionation reaction (step 2). It is therefore influenced by the size of the sulfur particles; the larger they are, the higher the plateau. Thus, this study proceeded with the lower size sulfur particles.

The active cathode material (viz. 19 μm sulfur powder with CNT) was mixed with Ketjen black and polyvinylidene difluoride at different mass ratios (e.g., 80:10:10, 70:20:10, 60:30:10, Figure S5). The formulated slurries were coated on aluminum mesh and carbon paper (Figures 2a and 2b, Figure S5). The coating follows the contours of the fibrous network (Figures 2c

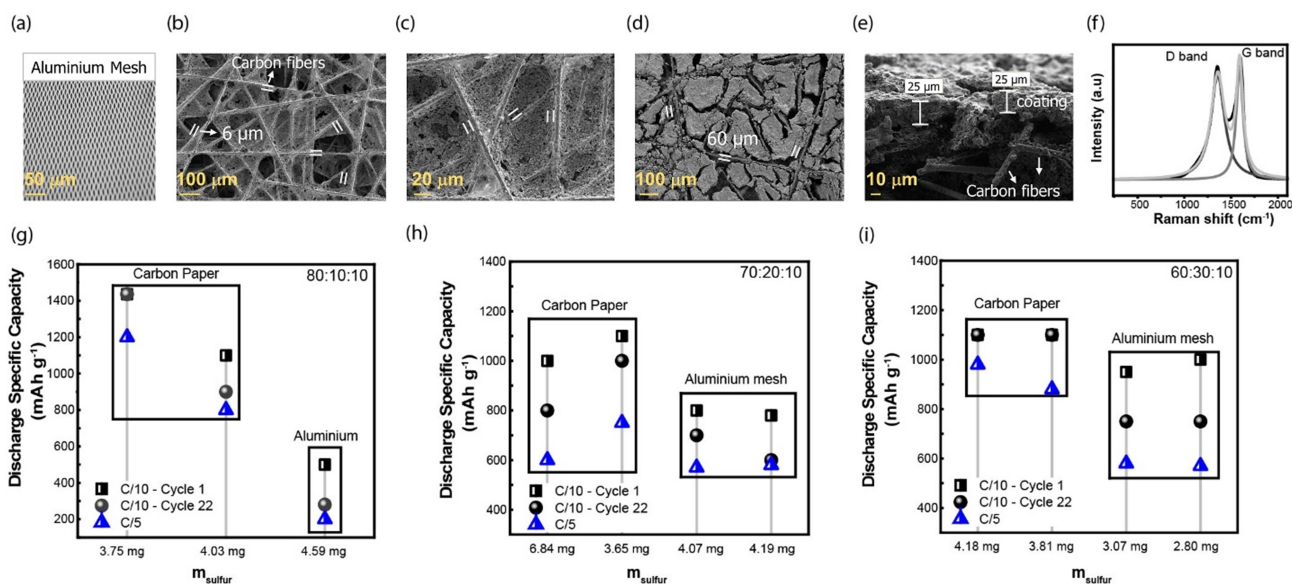


Figure 2. a) Optical image of an aluminum mesh collector. b) SEM micrograph showing the carbon paper network. c–e) SEM micrographs of the C/S slurry coating on the carbon paper. f) Raman spectroscopy of (e). Effect of current collector (carbon paper vs. aluminum) and active material mass (mass of sulfur on the electrode) on the performance of the Li–S cell. (S/C)/KB/PVDF cathode formulations 80:10:10 (g), 70:20:10 (h), 60:30:10 (i). The electrolyte comprises DOL/DME, 0.75 mol L⁻¹ LiTFSI, and 0.25 mol L⁻¹ LiNO₃. The operating temperature is 25 °C.

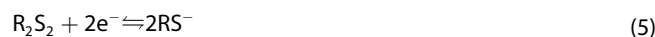
and 2d), unlike aluminum, where it remains at the surface. A cross-sectional SEM picture of the cathode with the carbon paper (Figure 2e, cathode formulation: (S/C)/KB/PVDF = 60:30:10) reveals a coating of ~20 μm and an areal loading equal to ~2.2 mAh cm⁻². The slurry is homogeneously distributed in the carbon network, and the space between the carbon fibers is filled with active material. Figure 2f shows the Raman spectra of the cathode, where two peaks are observed at 1590 and 1350 cm⁻¹. The peak at the greater wavenumber (G band) is assigned to the Raman active E_{2g} mode of the graphitic carbon lattice vibration, and the peak at 1350 cm⁻¹ (D band) corresponds to the A_{1g} mode of disordered carbon.^[5] The I_D/I_G ratio (viz. 1.83) suggests a high degree of graphitization and, in turn, high electronic conductivity. The sp²-hybridized carbon favors strong chemical interactions with sulfur, increasing the adsorption capability.^[36] The absence of peaks assigned to orthorhombic sulfur in the Raman spectra (between 300 and 500 cm⁻¹) further supports that sulfur is well dispersed and confined within the porous structure of the carbon material. The four-point probe measurements revealed a mean sheet resistance at 75.4 Ohmsq⁻¹, yielding a mean conductivity of 199.3 S m⁻¹ (Table S2).

What's more, the loading can be markedly enhanced (×6) by increasing the coating thickness to 250 μm to fill the whole electrode area. The volumetric capacity reaches ~1000 mAh cm⁻³ (~ $\frac{24.6 \text{ mAh}}{0.0255 \text{ cm}^3}$, Figure S6), markedly higher than other homologues (e.g., NMC is equal to 280 mAh cm⁻³^[5] while other S/C composites reach 689.4 mAh cm⁻³^[37]). The superior cycling performance of the cells having carbon paper as the current collector is evident in Figures 2g–i. The discharge specific capacities under C/5 and C/10 (1st and 22nd cycles) are consistently higher for different formulations and sulfur masses

at the cathode (m_{sulfur} ranging from 3.6 to 6.8 mg, where sulfur comprises 60% of m_{electrode}). Besides, they exhibit high capacity retention, owing to the high electronic conductivity of carbon paper (i.e., electrical resistivity is ca. 3 mΩ cm⁻²), which compensates for the natural resistance of sulfur and improves its adhesion during re-oxidation. The formulation containing 80% sulfur delivered the highest specific capacity (i.e., 1480 mAh g⁻¹) due to the higher cathode density. Sulfur has a higher tap density than Ketjen black and PVDF (i.e., ~1 > 0.1 and 0.5 g cm⁻³, respectively). Yet, the cell with a lower sulfur content (60%) delivers better performance (i.e., high capacity retention and superior specific capacity at a C/5 rate, Figure 2i) and is selected for the subsequent characterizations.

Phenyldisulfides and chalcogenides on the catholyte of the Li–S

The role of Ph₂S₂ as an additive in typical ether electrolyte(s) has been demonstrated before.^[20a,b] Ph₂S₂ mitigates the formation of soluble polysulfides (S_x²⁻, x > 4) and the shuttle phenomenon. At the same time, this electrochemically active species [given in Eq. (5)] boosts the gravimetric specific capacity in a standard ether-based electrolyte, as seen in Figure 3a.



The ether-based electrolyte associates well with Ph₂S₂ in a Li–S cell yielding a specific capacity of 1950 mAh g⁻¹ at C/5 (calculation provided below Figure S7), good electrochemical reversibility (ΔE = 2.61–2.57 at 0.1 mV s⁻¹), as well as temperature variability (70 cycles at 45 °C, Figure S7). There is a three-

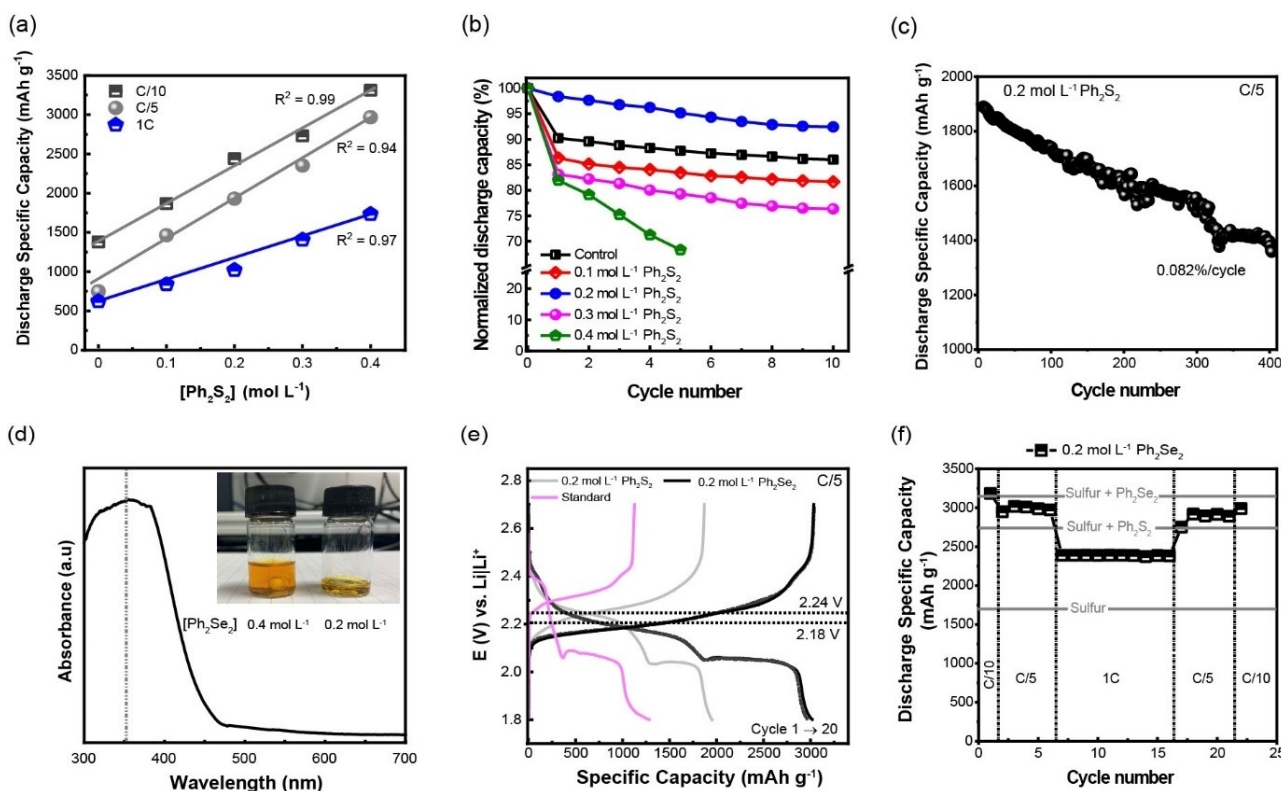


Figure 3. a) Effect of Ph_2S_2 concentration on the Li-S specific capacity at different C-rates. b) Normalized discharge capacity. c) Cyclability of the Li-S cell at a C/5 rate in an ether-based electrolyte with 0.2 mol L⁻¹ Ph_2S_2 . d) UV-Vis spectra of the phenyl diselenide solution in DOL/DME. Inset shows optical images of two solutions containing 0.4 and 0.2 mol L⁻¹ Ph_2S_2 in DOL/DME. e) Galvanostatic charge-discharge cycles of Li-S cells containing 0.2 mol L⁻¹ Ph_2S_2 . The results of cells containing 0.2 mol L⁻¹ Ph_2S_2 and the standard ether electrolyte are included for comparison purposes. f) Discharge-specific capacity at different C-rates for Li-S cells containing 0.2 mol L⁻¹ Ph_2S_2 in an ether-based electrolyte. The operating temperature is 25 °C.

fold increase in the specific capacity upon the addition of 0.4 mol L⁻¹ Ph_2S_2 (i.e., C-10 rate yields 3400 mAh g⁻¹), ascribed to the reactivity of the thiolate ions that serve as a chemical barrier in the solution toward the S_4^{2-} ions whilst being reduced. He et al.^[38] reported that elemental cyclooctasulfur is converted to long-chain polysulfides S_x^{2-} ($x=8, 6, 4$) during the first discharge where other polysulfides are barely detected (Figure S8 at a C/5 rate). The formed S_4^{2-} gets reduced to a meta-stable polysulfide species in the transition region between the discharge plateaus. However, in this case, R_2S_2 catalytically reduces the elemental sulfur to S_x^{2-} ($x < 4$) via an alternative route to the customarily observed “ring-opening” and “shortening” mechanism, that is, the conversion of S_8 to S_4^{2-} and S_3^{2-} .^[35] A detailed description of the different processes during the first discharge is given beneath Figure S8, following the analysis of our previous study.^[20b]

While the specific capacity increases with higher disulfide concentration (based on the 1st cycle), the results from the normalized capacity retention (for a total of 10 cycles) point to 0.2 mol L⁻¹ as the more suitable concentration (93.5% retention, Figure 3b). At this optimum Ph_2S_2 concentration (0.2 mol L⁻¹), typical GCD tests at a C/5 rate and room temperature demonstrated a 0.082% capacity loss per cycle (Figure 3c) for 400 cycles. Higher amounts of Ph_2S_2 lead to a relatively high energy density (i.e., 1853 Wh Kg⁻¹ at 0.4 mol dm⁻³ Ph_2S_2 , Fig-

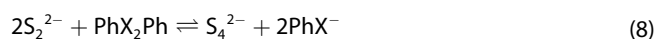
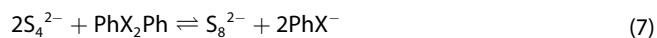
ure S8). However, at this concentration, the capacity of the cell is markedly diminished (i.e., >22% loss over 5 cycles, Figure 3b), attributed to concentration polarization losses and the fact that the ideal Ph_2S_2 concentration is related to the equilibrium constant that describes the reactivity of RS_2R and S_x^{2-} .^[27,39] The disulfides (and diselenides, for that matter) react with sulfur and hinder the formation of S_2^{2-} and S^{2-} as shown in Equation (6).



To further promote the redox mediation capability and accelerate the sulfur redox kinetics under practical conditions with high sulfur loading, low electrolyte volume, and slight lithium excess, we replaced the phenyldisulfide with another chalcogenide, namely selenium (Se).^[40] Similar to Ph_2S_2 , the selenium analogue Ph_2Se_2 is electrochemically active with a redox potential slightly lower than that of the former (i.e., $E_{\text{reduction PhSe}_2\text{Ph}} = -0.76$ V vs. Ag/AgCl and $E_{\text{oxidation PhSe}} = -0.36$ V vs. Ag|AgCl).^[40] The redox potential of this chalcogenide depends on the electron-withdrawing/donating nature of R in R_2S_2 . Selenium has similar chemical properties to sulfur, a lower theoretical specific energy (675 vs. 1.672 mAh g⁻¹), and is more electrically conductive (10^{-5} vs. 10^{-3} S cm⁻¹ for crystalline Se). Additionally, like sulfur, selenium needs a carbon host to

support its different phases and provide additional conductivity. Selenium poly-species can be trapped within the carbon matrix^[41] under various configurations, including spheres, fibers, irregular, and nanosheets that boost the cyclability of the LIS.^[42] However, it experiences a substantial volume change ($r_{\text{Se}} = 4.8 \text{ g cm}^{-3}$ vs. $r_{\text{Li}_2\text{Se}} = 2 \text{ g cm}^{-3}$) during electrochemical reduction. Most studies on selenium involve the formation of a carbon-selenium carbon (with the addition of sulfur in most cases). Herein, we avoid this fabrication process, which typically involves annealing temperatures, and add 0.2 mol L^{-1} Ph_2Se_2 to the standard ether-based electrolyte (in the same proportion as the work on Ph_2S_2 -ether catholyte). The broad absorbance peak at $\sim 370 \text{ nm}$ from the UV-vis spectra (Figure 3d) confirms the presence of polyselenides^[43] in the newly formulated electrolyte.

The specific capacity reaches 3000 mAh g^{-1} at a C/5 rate (Figure 3e) without decreasing the cell's open-circuit voltage at room temperature. The as-produced polyselenides (LiPhSePSs) improve the redox mediation capability, reduce the dissolution energy barrier, and increase the deposition dimension of Li_2S without damaging lithium metal during cycling, as demonstrated in Figures S9 and S10. Such a cell is cyclable at high C rates, achieving a specific capacity of 2400 mAh g^{-1} at 1C (Figure 3f), one of the highest reported for such a system in an ether electrolyte (Table S3). At each plateau, the formed polyselenides (i.e., organoselenates RSe^-) and polysulfide ions S_x^{2-} have a lifetime that depends on their i) electrochemical reactivity at the electrode surface (i.e., $\text{S}_4^{2-} \rightarrow \text{S}_2^{2-}$) and ii) chemical reactivity with the catholyte illustrated by the following reactions [Eq. (7) and (8)]:



Both plateaus are elongated (Figure 3e) as the chemical reaction becomes favorable because it maintains the non-reducible S_4^{2-} (or S_2^{2-}) ions until the dichalcogenides are exhausted. Experimental results and ab initio calculations confirm the strong interaction between Ph_2Se_2 and Li_2S , leading to cleavage of the Se–Se bond (172 kJ mol^{-1} as opposed to 240 kJ mol^{-1} for S–S) and the elongation of the Li–S bond in Li_2S .^[44]

Conclusion

Adjusting the sulfur content with its crystallinity (i.e., pretreatment procedure) was paramount for the robust performance of Li–S batteries. Herein, polymerized sulfur that stemmed from lengthy heat treatment at 160°C strongly bound to carbon (CNT, C/S slurry) and hindered the formation of S_2^- ions and Li_2S in favor of specific capacity retention and cyclability in a standard ether electrolyte. When applied to a carbon paper collector, the cathode slurry ((S/C)/KB/PVDF = 60:30:10, with a sulfur particle size of $19 \mu\text{m}$) homogeneously penetrated the pores of the current collector, giving an areal surface of

$\sim 2.2 \text{ mAh cm}^{-2}$ and a high volumetric capability of 1000 mAh cm^{-3} .

Striving towards higher specific capacities for this energy storage system, the suitability of polychalcogenide-based catholytes (PhX_2Ph ; $\text{X} = \text{S}, \text{Se}$) was established. At an optimal Ph_2S_2 concentration (0.2 mol L^{-1}), GCD tests at a C/5 rate and room temperature demonstrated a 0.082% capacity loss per cycle for 400 cycles and an energy density of 1853 Wh Kg^{-1} at 0.4 mol dm^{-3} Ph_2S_2 . Another cell containing 0.2 mol L^{-1} Ph_2Se_2 boosted further the capacity of the catholyte, reaching 2400 mAh g^{-1} (based on the mass of sulfur in the cathode) at a 1 C rate, one of the highest reported values for room temperature Li–S cells. These strategies for improving this room-temperature battery storage system are simple and effective and pave the way for future catholyte and cathode advances.

Acknowledgements

The authors would like to thank “La Région Centre Val de Loire” for financial support.

Conflict of Interest

The authors declare that they have no known competing financial interests or personal relationships that could have appeared to influence the work reported in this paper.

Data Availability Statement

Data that supports the findings of this study are available within the article.

Keywords: catholyte · diselenide · disulfide · Li–S battery · sulfur

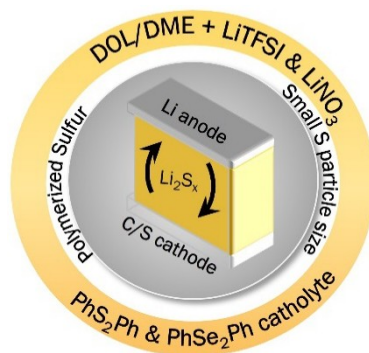
- [1] M. Aneke, M. Wang, *Appl. Energy* **2016**, *179*, 350–377.
- [2] G. Nikiforidis, M. Anouti, *Batteries & Supercaps* **2021**, *4*, 1708–1719.
- [3] A. Eftekhari, *ACS Sustainable Chem. Eng.* **2019**, *7*, 5602–5613.
- [4] J. Heelan, E. Gratz, Z. Zheng, Q. Wang, M. Chen, D. Apelian, Y. Wang, *JOM* **2016**, *68*, 2632–2638.
- [5] G. Nikiforidis, M. Raghbi, A. Sayegh, M. Anouti, *J. Phys. Chem. Lett.* **2021**, *12*, 1911–1917.
- [6] G. Nikiforidis, M. C. M. van de Sanden, M. N. Tsampas, *RSC Adv.* **2019**, *9*, 5649–5673.
- [7] N. Imanishi, O. Yamamoto, *Mater. Today. Adv.* **2019**, *4*, 100031.
- [8] G. Nikiforidis, G. J. Jongerden, E. F. Jongerden, M. C. M. van de Sanden, M. N. Tsampas, *J. Electrochem. Soc.* **2019**, *166*, A135–A142.
- [9] L. Carbone, T. Coneglian, M. Gobet, S. Munoz, M. Devany, S. Greenbaum, J. Hassoun, *J. Power Sources* **2018**, *377*, 26–35.
- [10] J. B. Robinson, K. Xi, R. V. Kumar, A. C. Ferrari, H. Au, M.-M. Titirici, A. Parra-Puerto, A. Kucernak, S. D. S. Fitch, N. Garcia-Araez, Z. L. Brown, M. Pasta, L. Furness, A. J. Kibler, D. A. Walsh, L. R. Johnson, C. Holc, G. N. Newton, N. R. Champness, F. Markoulidis, C. Crean, R. C. T. Slade, E. I. Andritsos, Q. Cai, S. Babar, T. Zhang, C. Lekakou, N. Kulkarni, A. J. E. Rettie, R. Jervis, M. Cornish, M. Marinescu, G. Offer, Z. Li, L. Bird, C. P. Grey, M. Chhowalla, D. D. Lecce, R. E. Owen, T. S. Miller, D. J. L. Brett, S. Liatard, D. Ainsworth, P. R. Shearing, *J. Phys. Energy* **2021**, *3*, 031501.
- [11] *Nat. Energy* **2022**, *7*, 461–461.10.

- [12] Y. Zhao, Y. Zhang, D. Gosselink, T. N. L. Doan, M. Sadhu, H.-J. Cheang, P. Chen, *Membranes* **2012**, *2*, 553–564.
- [13] S. Kandhasamy, G. Nikiforidis, G. J. Jongerden, F. Jongerden, M. C. M. van de Sanden, M. N. Tsampas, *ChemElectroChem* **2021**, *8*, 1156–1166.
- [14] S. Zhang, K. Ueno, K. Dokko, M. Watanabe, *Adv. Energy Mater.* **2015**, *5*, 1500117.
- [15] C. Luo, E. Hu, K. J. Gaskell, X. Fan, T. Gao, C. Cui, S. Ghose, X.-Q. Yang, C. Wang, *PNAS* **2020**, *117*, 14712–14720.
- [16] S. Yao, C. Zhang, F. Xie, S. Xue, K. Gao, R. Guo, X. Shen, T. Li, S. Qin, *ACS Sustainable Chem. Eng.* **2020**, *8*, 2707–2715.
- [17] a) M. Salama, Rosy, R. Attias, R. Yemini, Y. Gofer, D. Aurbach, M. Noked, *ACS Energy Lett.* **2019**, *4*, 436–446; b) Z. W. Seh, Y. Sun, Q. Zhang, Y. Cui, *Chem. Soc. Rev.* **2016**, *45*, 5605–5634.
- [18] a) Y. Son, J.-S. Lee, Y. Son, J.-H. Jang, J. Cho, *Adv. Energy Mater.* **2015**, *5*, 1500110; b) C. Zhang, Y. He, Y. Wang, Y. Liang, A. Majeed, Z. Yang, S. Yao, X. Shen, T. Li, S. Qin, *Appl. Surf. Sci.* **2021**, *560*, 149908; c) S. Yao, Y. He, Y. Wang, M. Bi, Y. Liang, A. Majeed, Z. Yang, X. Shen, *J. Colloid Interface Sci.* **2021**, *601*, 209–219.
- [19] a) S. Huang, Z. Wang, Y. Von Lim, Y. Wang, Y. Li, D. Zhang, H. Y. Yang, *Adv. Energy Mater.* **2021**, *11*, 2003689; b) Q. Pang, X. Liang, C. Y. Kwok, L. F. Nazar, *Nat. Energy* **2016**, *1*, 16132; c) M. Barghamadi, A. S. Best, A. I. Bhatt, A. F. Hollenkamp, M. Musameh, R. J. Rees, T. R  ther, *Energy Environ. Sci.* **2014**, *7*, 3902–3920.
- [20] a) S. Phadke, J. Pires, A. Korchenko, M. Anouti, *Electrochim. Acta* **2020**, *330*, 135253; b) S. Phadke, E. Coadou, M. Anouti, *J. Phys. Chem. Lett.* **2017**, *8*, 5907–5914; c) S. Chen, F. Dai, M. L. Gordin, Z. Yu, Y. Gao, J. Song, D. Wang, *Angew. Chem. Int. Ed.* **2016**, *55*, 4231–4235; *Angew. Chem.* **2016**, *128*, 4303–4307.
- [21] a) A. Korzhenko, P.-t. Skowron, P.-g. Schmitt, M. Anouti, **2021**; b) A. Korzhenko, P.-T. Skowron, P.-G. Schmitt, M. Anouti, *Arkema France, Fr.* **2019**, p. 77pp.; 171:470242 (FR).
- [22] D. Ainsworth, S. E. Rowlands, J. K. Kreis, L. A. Urrutia Mu  oz, *Vol. WO 2016/102942*, **2016**.
- [23] J. Zheng, M. Gu, M. J. Wagner, K. A. Hays, X. Li, P. Zuo, C. Wang, J.-G. Zhang, J. Liu, J. Xiao, *J. Electrochem. Soc.* **2013**, *160*, A1624–A1628.
- [24] K. R. Kim, S.-H. Yu, Y.-E. Sung, *Chem. Commun.* **2016**, *52*, 1198–1201.
- [25] B. Meyer, in *Advances in Inorganic Chemistry and Radiochemistry, Vol. 18* (Eds.: H. J. Emel  us, A. G. Sharpe), Academic Press, **1976**, pp. 287–317.
- [26] R. Steudel, O. Schumann, J. Buschmann, P. Luger, *Angew. Chem. Int. Ed.* **1998**, *37*, 2377–2378; *Angew. Chem.* **1998**, *110*, 2502–2504. [https://doi.org/10.1002/\(SICI\)1521-3773\(19980918\)37:17](https://doi.org/10.1002/(SICI)1521-3773(19980918)37:17).
- [27] G. Bosser, M. Anouti, J. Paris, *J. Chem. Soc. Perkin Trans. 2* **1996**, *9*, 1993–1999.
- [28] L. Zhang, Y. Ren, X. Liu, F. Han, K. Evans-Lutterodt, H. Wang, Y. He, J. Wang, Y. Zhao, W. Yang, *Sci. Rep.* **2018**, *8*, 4558.
- [29] Y. V. Mikhaylik, J. R. Akridge, *J. Electrochem. Soc.* **2004**, *151*, A1969.
- [30] J. J. Hu, G. K. Long, S. Liu, G. R. Li, X. P. Gao, *Chem. Commun.* **2014**, *50*, 14647–14650.
- [31] B. D. Adams, E. V. Carino, J. G. Connell, K. S. Han, R. Cao, J. Chen, J. Zheng, Q. Li, K. T. Mueller, W. A. Henderson, J.-G. Zhang, *Nano Energy* **2017**, *40*, 607–617.
- [32] Y. Liu, Y. Elias, J. Meng, D. Aurbach, R. Zou, D. Xia, Q. Pang, *Joule* **2021**, *5*, 2323–2364. <https://doi.org/10.1016/j.joule.2021.06.009>.
- [33] R. Fang, J. Xu, D.-W. Wang, *Energy Environ. Sci.* **2020**, *13*, 432–471. 10.1039/C9EE03408K.
- [34] M. Li, Z. Chen, T. Wu, J. Lu, *Adv. Mater.* **2018**, *30*, 1801190. <https://doi.org/10.1002/adma.201801190>.
- [35] M. Benaichouche, G. Bosser, J. Paris, J. Auger, V. Plichon, *J. Chem. Soc. Perkin Trans. 2* **1990**, 31–36.
- [36] K. Zhang, Q. Zhao, Z. Tao, J. Chen, *Nano Res.* **2013**, *6*, 38–46.
- [37] L. Wang, Y.-H. Song, B.-H. Zhang, Y.-T. Liu, Z.-Y. Wang, G.-R. Li, S. Liu, X.-P. Gao, *ACS Appl. Mater. Interfaces* **2020**, *12*, 5909–5919.
- [38] Q. He, A. T. S. Freiberg, M. U. M. Patel, S. Qian, H. A. Gasteiger, *J. Electrochem. Soc.* **2020**, *167*, 080508.
- [39] a) J. Robert, M. Anouti, J. Paris, *New J. Chem.* **1997**, *21*, 1187–1196 ; b) A. Ahrika, M. Anouti, J. Robert, J. Paris, *J. Chem. Soc. Perkin Trans. 2* **1998**, *3*, 607–610.
- [40] a) A. Ahrika, J. Robert, M. Anouti, J. Paris, *New J. Chem.* **2001**, *25*, 741–746; b) A. Ahrika, J. Robert, M. Anouti, J. Paris, *New J. Chem.* **2002**, *26*, 1433–1439.
- [41] V. H. Pham, J. A. Boscoboinik, D. J. Stacchiola, E. C. Self, P. Manikandan, S. Nagarajan, Y. Wang, V. G. Pol, J. Nanda, E. Paek, D. Mitlin, *Energy Storage Mater.* **2019**, *20*, 71–79.
- [42] a) H. Tian, H. Tian, S. Wang, S. Chen, F. Zhang, L. Song, H. Liu, J. Liu, G. Wang, *Nat. Commun.* **2020**, *11*, 5025; b) G.-L. Xu, J. Liu, R. Amine, Z. Chen, K. Amine, *ACS Energy Lett.* **2017**, *2*, 605–614.
- [43] Y. Xia, C. Lu, R. Fang, H. Huang, Y. Gan, C. Liang, J. Zhang, X. He, W. Zhang, *Electrochem. Commun.* **2019**, *99*, 16–21.
- [44] Q. Fan, B. Li, Y. Si, Y. Fu, *Chem. Commun.* **2019**, *55*, 7655–7658.

Manuscript received: May 23, 2022
Revised manuscript received: July 4, 2022
Accepted manuscript online: July 4, 2022

RESEARCH ARTICLE

What is key: Performance parameters affecting the specific capacity and long-term performance of Li–S batteries were investigated. From tweaking the sulfur nature in the cathode to trapping the polysulfide ions to formulate catholytes with phenyl-dichalcogenide (PhX_2Ph ; $\text{X}=\text{S}, \text{Se}$), this study provided the important role of both catholyte and nature of cathode's sulfur on record-specific capacity (3000 mAh g^{-1} at a C/5) and high energy density (1853 Wh Kg^{-1}).



*Dr. G. Nikiforidis, Dr. J. Pires, Dr. S. Phadke, Prof. M. Anouti**

1 – 9

Effective Ways to Stabilize Polysulfide Ions for High-Capacity Li–S Batteries Based on Organic Chalcogenide Catholytes

